Antoinette M. Maniatty[1]
Professor
Fellow of ASME
Department of Mechanical, Aerospace, and Nuclear Engineering,
Rensselaer Polytechnic Institute,
110 8th Street,
Troy, NY 12180
e-mail: maniaa@rpi.edu

G. S. Cargill III
Professor Emeritus
e-mail: gsc3@lehigh.edu

Laura E. Moyer[2]

Department of Materials Science and Engineering,
Lehigh University,
5 East Packer Avenue,
Bethlehem, PA 18015

Chia-Ju Yang
Department of Mechanical, Aerospace, and Nuclear Engineering,
Rensselaer Polytechnic Institute,
110 8th Street,
Troy, NY 12180

Investigation of Thermal Stress Variability Due to Microstructure in Thin Aluminum Films

An X-ray microbeam study and a polycrystal finite element model of a 10×10 μm^2 section of a 1 μm thick polycrystalline aluminum film on a silicon substrate are used to investigate the effect of microstructure on thermal stress variability. In the X-ray microbeam study, the grain orientations and deviatoric elastic strain field are measured at the subgrain level in the film during and after two thermal cycles. A finite element model of the observed grain structure is created and modeled with an elastoviscoplastic crystal constitutive model that incorporates film thickness and grain size effects as well as dislocation entanglement hardening. The experimental and simulation results are compared at both the film and subgrain scales. While the experiment and model agree fairly well at the film level, the experimental results show much greater elastic strain variability than the simulations. In considering the grain size effect, the experiment and model both predict a similar Hall–Petch coefficient, which is consistent with literature data on free standing aluminum thin films. [DOI: 10.1115/1.4002212]

1 Introduction

Thin metal films have been widely studied to gain a better understanding of the mechanical properties of conductor lines or electrical interconnects used in integrated circuits. Thin film properties are considerably different from bulk material properties because of the strong effect of the surface interfaces and microstructural level heterogeneities, such as grain structure and orientations, which have a similar size scale to the film thickness [1]. In particular, thin films have a much higher yield stress than the bulk material and the strength of films has been observed to increase with decreasing film thickness and grain size [2–4]. The most common materials used for interconnects and, thus, the most often studied as thin films, are aluminum (Al) and copper (Cu) due to their low resistivity.

Thermal stresses develop in interconnects during fabrication and in operation at elevated temperatures due to the large difference in the coefficient of thermal expansion between interconnects and their surrounding layers. These stresses can lead to failure of devices due to the formation of voids and hillocks in interconnects [5]. At elevated temperatures, metallization films are in compression since the thermal expansion coefficient of the metallic film is higher than the surrounding nonmetallic materials. These compressive stresses relax due to inelastic deformation and it is during inelastic deformation that hillocks or protrusions on the surface of the film form. Several mechanisms are thought to be active during stress relaxation at elevated temperatures including grain boundary diffusion and dislocation glide and climb [6,7]. Because thin metal films typically have a columnar grain structure with all grain boundaries perpendicular to the film plane, grain boundary diffusion is limited compared with that in bulk materials and dislocation motion remains the primary mechanism for inelastic deformation even at elevated temperatures. If the film does not have a stable grain size, grain growth may also occur and increases the likelihood of hillock formation considerably [8]. At lower temperatures, dislocation glide is the dominant mechanism of inelastic deformation. The orientation of the grains also has a significant effect on the thermal stresses and resulting hillock formation. Al and other face-centered cubic (FCC) metallic films typically have a strong $\langle 111\rangle$ fiber texture where the $\langle 111\rangle$ crystal direction tends to be in the normal direction to the film plane. Hillocks have been observed to form primarily in grains oriented away from the dominant $\langle 111\rangle$ texture [9–11].

With X-ray diffraction, it is possible to measure strain and to determine the texture of thin films. Traditionally, only average strain values have been obtained due to large X-ray beam sizes, typically several millimeters, compared with the average grain size of the sample and to the sizes of conductor lines [1,12]. Grain sizes of thin films are typically on the order of the film thickness, in the micron or submicron range. Dimensions of conductor lines are also in this range. Over the last 15 years, microbeam X-ray diffraction, which uses a beam diameter of less than 1 μm, has been developed to allow single grain or even subgrain strain and orientation analysis in many thin films and conductor lines [13–15].

Dislocation mechanisms are the primary source of strengthening in thin metallic films and studying and modeling these mechanisms in order to better understand and predict the behavior of thin metallic films has been a topic of on-going research over the

[1]Corresponding author.
[2]Present address: Alcoa Power and Propulsion, Alcoa, Inc., 9 Roy St., Dover, NJ 07801.

Contributed by the Applied Mechanics of ASME for publication in the Journal of Applied Mechanics. Manuscript received March 24, 2010; final manuscript received July 8, 2010; accepted manuscript posted July 23, 2010; published online October 20, 2010. Editor: Robert M. McMeeking.

 Copyright © 2011 by ASME

Downloaded 08 Dec 2010 to 128.113.218.67. Redistribution subject to ASME license or copyright; see http://www.asme.org/terms/Terms_Use.cfm

past 2 decades. The interaction of dislocations with the layers surrounding the thin film as well as with grain boundaries and other dislocations are the primary sources of strengthening. Nix [5], following the work of Freund [16] on misfit dislocations in epitaxial films, derived a film thickness effect on strengthening by considering the additional energy required to move a dislocation in a thin film due to the creation of misfit dislocations in the interfaces of the film and the surrounding layers. In recent years, to better understand the effect of dislocation interactions in thin films, dislocation dynamics simulations have been used [17–19].

Crystal plasticity models can be used to characterize the effect of grain orientations on the thermal stress. Such an approach was taken by Povirk et al. [20] who studied the effect of orientation on thermal stresses in Al interconnects where a section of an Al interconnect was modeled as an elliptic single crystal embedded in silicon using the Eshelby theory for ellipsoidal inclusions [21]. A crystal plasticity model developed for bulk materials was used in that work. A crystal plasticity model that incorporated the film thickness effect on the slip systems proposed by Nix [5], as well as a grain size effect and dislocation entanglement hardening, was used by Yu et al. [22] to study the effect of grain orientations on thermal stresses in thin films. In that work, single crystals of different orientations were subjected to equal biaxial strains associated with thermal cycles, assuming uniform strains in the film, and the resulting stresses were computed. Macroscale stresses were computed by averaging the stresses for a reasonable distribution of grain orientations. The predicted macroscale stresses agreed fairly well with the experimental data over a range of film thicknesses and grain sizes. The variability in the grain scale stress due to the grain orientation was predicted to be substantial. By assuming equal biaxial strains in each grain, compatibility is satisfied but equilibrium is violated across grain boundaries. A discrete finite element model of a thin film grain structure, which is developed in this work and described next, satisfies both equilibrium and compatibility by allowing intragranular strain and stress heterogeneities.

In this work, microbeam X-ray diffraction and a discrete polycrystal model are used to investigate the variability of stresses, due to microstructural variability, in a 1 μm thick polycrystalline Al film on a silicon (Si) substrate. In the experiment, the polycrystalline Al film on the Si substrate was subjected to a sequence of two thermal cycles and the orientations and elastic, deviatoric strains were measured using X-ray microdiffraction on a 10×10 μm^2 area both during the thermal cycles and eight consecutive times after the second cycle. In order to better understand the effect of grain orientations and grain size on the local elastic strains and to test the validity of our grain scale model, we model the 10×10 μm^2 area scanned subjected to the measured temperature history. A model columnar grain structure is defined based on the eight area scans taken after the second thermal cycle. A finite element model of this grain structure where the grains are modeled with an elastoviscoplastic crystal constitutive model that accounts for dislocation interactions with other dislocations, the substrate, grain boundaries, and an oxide capping layer, is subjected to the experimentally measured temperature history. At the film scale (macroscale), the average predicted stresses are compared with the average measured stresses. The effect of grain orientation and size is investigated at the grain scale.

2 Experimental

The sample consisted of a 1 μm Al film on a 250 μm Si substrate. There was a 3000 Å, SiNx layer between the Al film and the Si substrate to improve adhesion and fiber texture. The Al film was deposited onto the Si substrate by e-beam evaporation in a vacuum of 10^{-8} torr with an evaporation rate of 3 nm/s and with the substrate at room temperature. After deposition, the sample was annealed at 300°C for one hour. Figure 1(*a*) shows a focused ion beam (FIB) image of the resulting grain structure. The average in-plane grain size for the film was approximately 2.3 μm with some grains as large as 4 μm. The sample had a strong ⟨111⟩ fiber texture, as shown by the pole figure in Fig. 1(*b*). Note that the sample coordinates *x* and *y* are in the film plane and *z* is taken as the out of plane coordinate. A 3.5×14 mm^2 portion of the wafer was cut and used as the sample in the experiments.

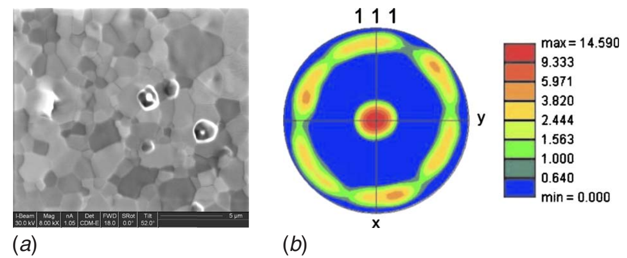

Fig. 1 (*a*) FIB image showing the grain structure of the Al film and (*b*) pole figure showing the strong ⟨111⟩ fiber texture

The X-ray microdiffraction measurements were performed at the Advanced Photon Source, Argonne National Laboratory (Argonne , IL), using the University-National Laboratory-Industry Collaborative Access Team (UNICAT) 34-ID beamline. The beam size was approximately 0.5×0.5 μm^2 and the step sizes for each 10×10 μm^2 area scan were 0.5 μm in the *x*-direction and 1.0 μm in the *y*-direction. The larger step size was used in the *y*-direction because of beam spreading that occurs in that direction due to the tilt of the sample. The grain orientation and elastic, deviatoric strain were determined at each location using the method described in Ref. [14].

The sample was subjected to a series of two thermal cycles, during and after which X-ray microdiffraction was used to measure both the local grain orientations and the elastic, deviatoric strains on a 10×10 μm^2 area. To accomplish this, the sample was mounted on a chip carrier that fit into a specially designed heating stage for in situ X-ray microdiffraction. The arm and the sample clips of the stage were made of INVAR 36 (steel alloy with 36% nickel), which has a low thermal expansion coefficient of $1.64 \times 10^{-6}/°C$, to minimize sample movement caused by temperature changes. The heat source was a 250 μm diameter Nichrome (80% Ni, 20% Cr) wire that was inlaid into a ceramic part of the stage where the chip carrier was mounted and heated the sample from below when a voltage was applied. The temperature was monitored using two thermocouples, one inside the ceramic and one directly in contact with the sample. First, two area scans were performed at room temperature. Then, the sample was heated to 300°C in 50°C increments, except for the first increment from room temperature (25°C) to 50°C. After each 50°C increment, two area scans were obtained including at 300°C. The sample was then cooled to room temperature and the process was repeated. No area scans were taken during cooling. After the second thermal cycle, eight area scans were obtained at room temperature. Because of the time required to take the area scans during the heating legs, the overall heating sequence took approximately 27 h while cooling took only about 0.5 h, not including the time for the area scans performed after reaching room temperature. The temperature history for the second cooling leg is shown in Fig. 2.

3 Film Model

3.1 Grain Structure Model. The grain orientations obtained from the eight 10×10 μm^2 area scans taken at the end of the second thermal cycle at room temperature are used to define the model grain structure. The first three area scans are shown in Fig. 3 using in-plane [100] inverse pole figure color maps and depicting grain boundaries greater than 5 deg. While the texture exhibits a strong ⟨111⟩ fiber texture out of the plane along the *z*-direction (Fig. 1(*b*)), the in-plane texture is more varied but not random

Downloaded 08 Dec 2010 to 128.113.218.67. Redistribution subject to ASME license or copyright; see http://www.asme.org/terms/Terms_Use.cfm

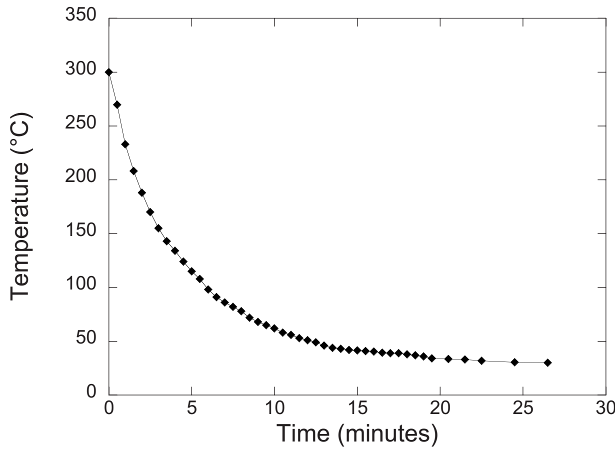

Fig. 2 Measured temperature history for the second cooling leg

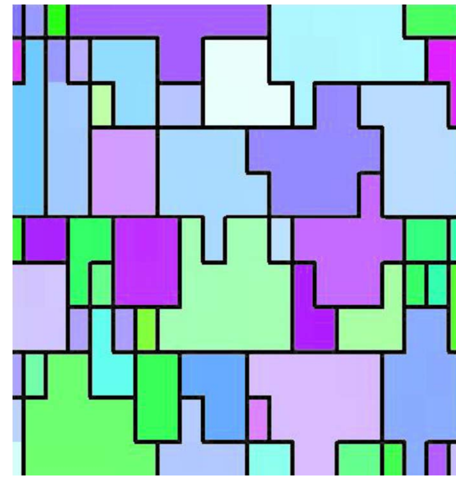

Fig. 4 [100] inverse pole figure color map of grain structure model used in simulations

with the [100] sample direction (x) tending away from ⟨001⟩ crystal directions. Although there are some similarities between the orientation color maps, they are not identical, probably because of small position drifts during the measurements and because of measurement errors as discussed below.

In order to define a model grain structure that represents well the observed grain structures, we first register the images and then take the grain orientation at each pixel that is most common among the eight area scans. The registration process is to compensate for potential sample drift between the scans. We only considered potential rigid translations in x and y.

To define the difference between images, we use the Euclidean difference of the quaternion representations of the orientations after compensating for cubic symmetry transformations. See, for example, the work of Cho et al. [23] for details about quaternion representations and operations. We use this minimized Euclidean difference, averaged over the whole area scan, to define the difference between scans. We find the difference between scans where the pixel positions between the scans are either the same or offset by one pixel in either x or y. The result is that scans 2–8 match best with no offset and scan 1 matches the rest if the pixels of scan 1 are moved down one position in y relative to the other scans.

Finally, to define a representative grain structure from the eight registered images, we took the orientation that occurred most frequently at each pixel location. The resulting grain structure used in the model is shown in Fig. 4.

3.2 Constitutive Model. A small strain, thermo-elastoviscoplastic crystal model is used to model the behavior of the aluminum grains in the film during the thermal cycle. The model is a small strain version, with minor modifications, of that described by Yu et al. [22] and is summarized here. The model assumes an additive decomposition of the strain into thermal, elastic, and plastic parts

$$\boldsymbol{\varepsilon} = \boldsymbol{\varepsilon}^{\theta} + \boldsymbol{\varepsilon}^{e} + \boldsymbol{\varepsilon}^{p} \tag{1}$$

where $\boldsymbol{\varepsilon}$ is the small strain tensor and superscripts θ, e, and p indicate the thermal, elastic, and plastic parts, respectively. The thermal expansion is isotropic for cubic crystals, thus,

$$\boldsymbol{\varepsilon}^{\theta} = \int_{\theta_o}^{\theta} \alpha(\theta') d\theta' \boldsymbol{I} \tag{2}$$

where α is the temperature dependent coefficient of thermal expansion, $\boldsymbol{I}$ is the identity tensor, and θ and θ_o are the current and reference temperatures, respectively. The elastic behavior for crystals with cubic symmetry can be expressed as

$$\boldsymbol{\sigma} = 2\mu\boldsymbol{\varepsilon}^{e} + \lambda\ tr(\boldsymbol{\varepsilon}^{e}) - 2\eta\boldsymbol{\Xi}[\boldsymbol{\varepsilon}^{e}] \tag{3}$$

where μ, λ, and η are the temperature dependent elastic parameters that can be related to the classically defined elastic stiffness parameters as $\mu = C_{44}$, $\lambda = C_{12}$, and $2\eta = 2C_{44} + C_{12} - C_{11}$ and $\boldsymbol{\Xi}$ is a fourth order tensor defined with respect to the lattice coordinates such that $\Xi_{ijkl} = 1$ if $i=j=k=l$ and $\Xi_{ijkl} = 0$ otherwise. The plastic deformation is assumed to be due to slip along the 12 primary {111} ⟨110⟩ crystallographic slip systems, thus,

$$\dot{\boldsymbol{\varepsilon}}^{p} = \frac{1}{2}\sum_{\beta=1}^{12} \dot{\gamma}^{\beta}(\boldsymbol{s}^{\beta} \otimes \boldsymbol{m}^{\beta} + \boldsymbol{m}^{\beta} \otimes \boldsymbol{s}^{\beta}) \tag{4}$$

where $\dot{\gamma}^{\beta}$ is the rate of shearing and $\boldsymbol{s}^{\beta}$ and $\boldsymbol{m}^{\beta}$ are the slip direction and slip plane normal, respectively, for the β slip system and

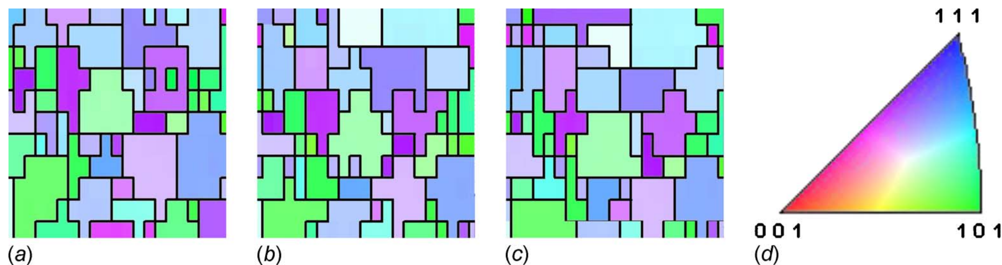

Fig. 3 [100] inverse pole figure color maps of first three area scans at room temperature after the second thermal cycle. Grain boundaries greater than 5 deg are shown and x and y are the horizontal and vertical directions, respectively.

Downloaded 08 Dec 2010 to 128.113.218.67. Redistribution subject to ASME license or copyright; see http://www.asme.org/terms/Terms_Use.cfm

$\otimes$ indicates dyadic product. The rate of shearing on the each slip system $\dot{\gamma}^\beta$ is related to the resolved shear stress on that slip system, $\tau^\beta = \boldsymbol{s}^\beta \cdot (\boldsymbol{\sigma m}^\beta)$, using a standard power law

$$\dot{\gamma}^\beta = \dot{c} \left| \frac{\{|\tau^\beta| - \tau_g^\beta\}}{g^\beta} \right|^{1/m} sgn(\tau^\beta) \qquad (5)$$

where $\dot{c}$ is a material parameter, τ_g^β is the stress that needs to be overcome to move a dislocation while accommodating geometric constraints between the grain and its surroundings (substrate, oxide layer, and neighboring grains), g^β is the resistance to dislocation motion associated with dislocation entanglement, and m is the strain rate sensitivity. Also in the above equation, $\{\cdot\}$ are Macaulay brackets defined such that $\{x\}=0$ if $x \leq 0$ and $\{x\}=x$ if $x>0$, and sgn is the sign function to ensure that $\dot{\gamma}^\beta$ and τ^β have the same sign. The temperature dependent strain rate sensitivity is calculated by the formula suggested by Kocks [24]

$$m = \frac{9k\theta}{b_B^3 \sqrt{\mu(\mu - \eta)}} \qquad (6)$$

where k is the Boltzmann constant and b_B is the Burgers vector.

The term τ_g^β consists of two parts, one associated with the stress required to lay down misfit dislocations between the film and substrate and between the film and oxide layer forming on top of the film that captures the effect of the film thickness and the other one associated with interactions with neighboring grains that captures the effect of the grain size. The film thickness effect is based on the work of Nix [5] and the grain size effect is based on the work of Ashby [25]. The resulting equations are

$$\tau_g^\beta = \tau_{ft}^\beta + \tau_{gs}^\beta \qquad (7)$$

$$\tau_{ft}^\beta = \frac{b_B \sin \phi^\beta}{2\pi(1-\nu)h} \left[\frac{\mu\mu_s}{\mu + \mu_s} \ln\left(\frac{h}{b_B}\right) + \frac{\mu\mu_o}{\mu + \mu_o} \ln\left(\frac{t}{b_B}\right) \right] \qquad (8)$$

$$\tau_{gs}^\beta = \frac{\mu}{\pi(1-\nu)} \sqrt{\frac{b_B \rho^\beta}{d}} \qquad (9)$$

where ϕ^β is the angle between the normal to the film and the normal to the β slip system, ν is Poisson's ratio for the film, h is the film thickness, μ_s and μ_o are the shear moduli for the substrate and oxide layer, respectively, t is the thickness of the oxide layer, and d is the grain size. It should be noted that the elastic behavior of the film is approximated as isotropic in Eqs. (8) and (9), which is a reasonable approximation for aluminum crystals. The parameter ρ^β is associated with the amount of slip but including a recovery term and takes on the form

$$\dot{\rho}^\beta = |\dot{\gamma}^\beta| - r\rho^\beta \exp\left(\frac{-Q}{R\theta}\right) \qquad (10)$$

where Q is the activation energy for recovery, which is taken to be associated with grain boundary diffusion [26], R is the ideal gas constant, and r is a material parameter associated with the rate of recovery.

The resistance to slip g^β represents slip system hardening due to dislocation-dislocation interactions and evolves according to the model given in Bassani and Wu [27] with a recovery term added and is summarized as follows:

$$g^\beta = g_o(\theta) + \int_0^t \dot{g}^\beta dt \qquad (11)$$

$$\dot{g}^\beta = \dot{g}_h^\beta + r\left(1 - \frac{g^\beta}{g_o}\right) \exp\left(\frac{-Q}{R\theta}\right) \qquad (12)$$

$$\dot{g}_h^\beta = h_\beta |\dot{\gamma}^\beta| \qquad (13)$$

Table 1 Material parameters

$\dot{c}$	0.001 s^{-1}
ν	0.31
Q	90 kJ/mol
h_o	$7.0g_o$
h_s^{III}	$1.0g_o$
γ_o^I	0.001
b_B	0.283 nm
μ_o	178.9 GPa
r	3×10^5 s^{-1}
h_s^I	$1.5g_o$
g_I	$1.3g_o$
γ_o^{III}	0.075

$$h_\beta = \left[(h_o - h_s) \operatorname{sech}^2\left(\frac{(h_o - h_s)\rho^\beta}{g_I - g_o}\right) + h_s \right] \left[1 + \sum_{\xi=1}^{12} f_{\beta\xi} \tanh\left(\frac{\rho^\xi}{\gamma_o^I}\right) \right] \qquad (14)$$

$$h_s = h_s^I + (h_s^{III} - h_s^I) \tanh\left(\frac{\rho}{\gamma_o^{III}}\right), \quad \rho = \sum_{\beta=1}^{12} \rho^\beta \qquad (15)$$

where g_o is the reference annealed value of g at a given temperature, the matrix $f_{\beta\xi}$ are amplitude factors, which are reported in Bassani and Wu [27] and h_o, g_I, γ_o^I, γ_o^{III}, h_s^I, and h_s^{III} are the material parameters. These parameters for pure aluminum are reported by Povirk et al. [20].

The temperature dependent model parameters used here are given below and all the other parameters are listed in Table 1. The thermal expansion coefficients for both the aluminum film α and the silicon substrate α_s are from Touloukian et al. [28] and Touloukian et al. [29] and the elastic parameters for each are found in Every and McCurdy [30]. The parameters for the aluminum film crystal plasticity model are from Povirk et al. [20] and the activation energy Q is from Frost and Ashby [26]. The only parameter in this model not taken from literature is r in Eqs. (10) and (12) associated with the rate of recovery, which is chosen to best match thermal cycle data.

$$\alpha = 2.337 \times 10^{-5} - (6.559 \times 10^{-9})\theta + (2.480 \times 10^{-11})\theta^2 \qquad (16)$$

$$\alpha_s = 1.877 \times 10^{-6} + (3.868 \times 10^{-9})\theta - (1.360 \times 10^{-12})\theta^2 \qquad (17)$$

$$g_o = -3.8144 + 0.12503\theta - 3.0871 \times 10^{-4}\theta^2 + 2.0481 \times 10^{-7}\theta^3 \qquad (18)$$

$$C_{11} = 116{,}280 - 30.878\theta \qquad (19)$$

$$C_{12} = 59{,}490 + 2.892\theta \qquad (20)$$

$$C_{44} = 32{,}850 - 15.76\theta \qquad (21)$$

$$\mu_s = 81{,}000 - 6.25\theta \qquad (22)$$

where θ is in K, α, and α_s are in K^{-1} and g_o, C_{11}, C_{12}, C_{44}, and μ_s are in MPa.

3.3 Finite Element Model. The film is modeled with a 3D finite element model where the governing equations are the equilibrium and strain equations together with the constitutive equations described in the preceding section subjected to displacement and traction boundary conditions as follows:

$$\operatorname{div} \boldsymbol{\sigma} = 0 \quad \text{in } \Omega \qquad (23)$$

Downloaded 08 Dec 2010 to 128.113.218.67. Redistribution subject to ASME license or copyright; see http://www.asme.org/terms/Terms_Use.cfm

$$\boldsymbol{\varepsilon} = \frac{1}{2}(\nabla \boldsymbol{u} + \nabla(\boldsymbol{u})^T) \quad \text{in} \ \ \Omega \tag{24}$$

$$\boldsymbol{e}_i \cdot \boldsymbol{u} = \hat{u}_i \quad \text{on} \quad \partial\Omega_{1i} \tag{25}$$

$$\boldsymbol{e}_i \cdot \boldsymbol{\sigma n} = 0 \quad \text{on} \quad \partial\Omega_{2i} \tag{26}$$

where $\boldsymbol{u}$ is the displacement field, $\boldsymbol{n}$ is the outward unit normal on the boundary of the film $\partial\Omega$, Ω is the region the film occupies, and $\boldsymbol{e}_i$ are unit vectors associated with the sample coordinates. The top of the film was treated as traction free, Eq. (26). The substrate is not explicitly modeled but is assumed to be perfectly bonded to the film and relatively thick compared with the film, so that the deformation of the substrate is solely due to thermal strain and not influenced by the film. Thus, a displacement boundary condition on the bottom face of the film ($\partial\Omega_b$) in contact with the substrate is applied such that

$$\hat{u}_i = \boldsymbol{e}_i \cdot \boldsymbol{\varepsilon}_s^{\theta}(\boldsymbol{x} - \boldsymbol{x}_o) \quad \boldsymbol{x} \in \partial\Omega_b \tag{27}$$

in the directions tangent to the film plane, x and y, and $\hat{u}_z=0$ in the the normal direction, where $\boldsymbol{\varepsilon}_s^{\theta}$ is the thermal strain in the silicon defined in the same way as in the aluminum, Eq. (2), but using the thermal expansion coefficient for silicon, Eq. (17), and $\boldsymbol{x}_o \in \partial\Omega_b$ is a reference location. The boundary conditions on the lateral faces are defined such that the faces remain perpendicular to the bottom face, moving in the normal direction with the bottom face, and traction free in the tangential directions. This last boundary condition is based on the fact that the lateral faces are in contact with surrounding film material that is also bonded to the substrate but with unknown microstructure.

The finite element implementation involves integrating the constitutive equations described in the preceding section for the given total and thermal strain increments and the solution of the nonlinear system of equations resulting from discretizing the governing equations. The constitutive model is integrated by a fully implicit radial return mapping algorithm [31] and a corresponding consistent tangent formulation is used with a standard Newton–Raphson method for solving the nonlinear system of equations resulting from the finite element discretization. For details, see the work of Yang [32].

The film is modeled with 231 20-node quadratic hexahedral elements. One element per pixel is used and one element through the thickness. Thus, the elements are each $0.5 \times 1 \times 1 \ \mu\text{m}^3$. Each element is assigned with the orientation associated with that pixel as described in Sec. 3.1.

4 Results and Discussion

4.1 Macroscale Response. First, we compare the predicted and experimentally measured macroscale (average) responses for the second thermal cycle. We compare the second thermal cycle because it is less affected by prior history. In the model, the film is treated as initially stress free at 300°C. For the experiment, since only the deviatoric elastic strains are measured, only the deviatoric stresses can be computed. However, since the top surface is stress free, the average stress is expected to be such that $\langle \sigma_{zz} \rangle = 0$, where angle brackets $\langle \cdot \rangle$ indicates the mean average over all the pixels in a scan. This allows the average hydrostatic stress $\langle \sigma_h \rangle$ to be determined in terms of the deviatoric stresses as

$$\langle \sigma_h \rangle = \langle -\sigma'_{zz} \rangle = \langle \sigma'_{xx} + \sigma'_{yy} \rangle \tag{28}$$

where σ'_{ij} are the deviatoric stress components. The average biaxial stress is then computed from

$$\langle \sigma_b \rangle = \frac{1}{2}(\langle \sigma_{xx} \rangle + \langle \sigma_{yy} \rangle) = \frac{3}{2}(\langle \sigma'_{xx} \rangle + \langle \sigma'_{yy} \rangle) \tag{29}$$

The average biaxial stress versus the temperature is plotted in Fig. 5. At close to room temperature, the simulation and experiments are in very good agreement, however, at elevated temperatures, the simulation does not fully capture the recovery. This is likely due to the additional relaxation mechanisms, in particular, that is due to the material migration via grain boundary diffusion, which is not included in the model.

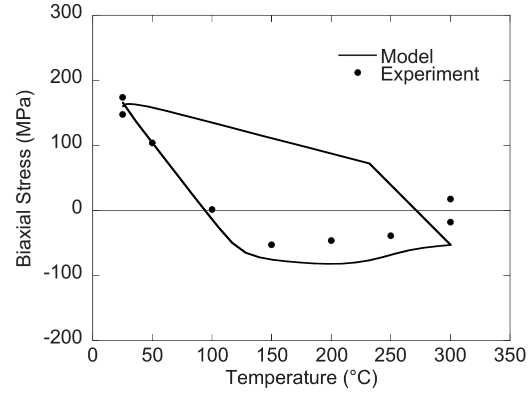

Fig. 5 Comparison between the model and the experiment of the average biaxial stress versus temperature

4.2 Grain Scale Variability. To compare the model results on the grain scale with the experimental result, we first try to separate the level of variability in the deviatoric elastic strain measurements due to measurement error from that truly present due to microstructural variations. This can best be done by investigating the strains at the end of the second thermal cycle since we have a set of eight measurements. First, we remove from the data measurements where the pixel deviation is greater than 0.5 to remove the data with greatest error and outliers. The pixel deviation is the deviation between the indexed peaks from the X-ray microdiffraction and the optimized peaks (least-squares fit) when there are more than four indexed peaks (the minimum number required for determining the deviatoric elastic strain). There were always more than six indexed peaks. After removing these data, there were still at least three measurements of deviatoric elastic strain at each pixel with most pixels having typically seven measurements, i.e., from seven of the eight scans. Also note, because the first scan is translated downward one pixel in registration, there were no data from that scan for the top row of pixels.

Next, we adjusted the strain level in scans 2–8 to compensate for relaxation, so that the resulting deviatoric elastic strains of these scans could be directly compared. Figure 6(*a*) shows the average deviatoric elastic normal strain components for each scan. Note, the average shear strain components are relatively small and not shown. The relaxation that occurs at room temperature over the time it takes for each scan is evident. To compensate for this, we assume the relaxation is proportional for all strain components and we adjust the deviatoric elastic strain data in scans 2–8 to match the average deviatoric elastic strain component $\langle \varepsilon_{zz}^{e'} \rangle$. The components of scans 2–8, at each pixel p are adjusted according to

$$(\varepsilon_{ij}^{e'})_{ps} = \frac{\langle \varepsilon_{zz}^{e'} \rangle_1^m}{\langle \varepsilon_{zz}^{e'} \rangle_s^m} (\varepsilon_{ij}^{e'})_{ps}^m \tag{30}$$

where subscripts p and s indicate pixel and scan, respectively, and superscript m indicates measured value. The resulting average normal deviatoric elastic strain components are shown in Fig. 6(*b*).

Now, we look at the variability in the deviatoric elastic strains between the scans. This represents the measurement error if we assume the microstructure is not changing and the adjustment for relaxation is valid. We focus on the perpendicular deviatoric elastic strain $\varepsilon_{zz}^{e'}$. To simplify notation, let $\varepsilon_{ps} = (\varepsilon_{zz}^{e'})_{ps}$ at pixel p in scan s. For each pixel p, we can compute the average $\bar{\varepsilon}_p$ and

Downloaded 08 Dec 2010 to 128.113.218.67. Redistribution subject to ASME license or copyright; see http://www.asme.org/terms/Terms_Use.cfm

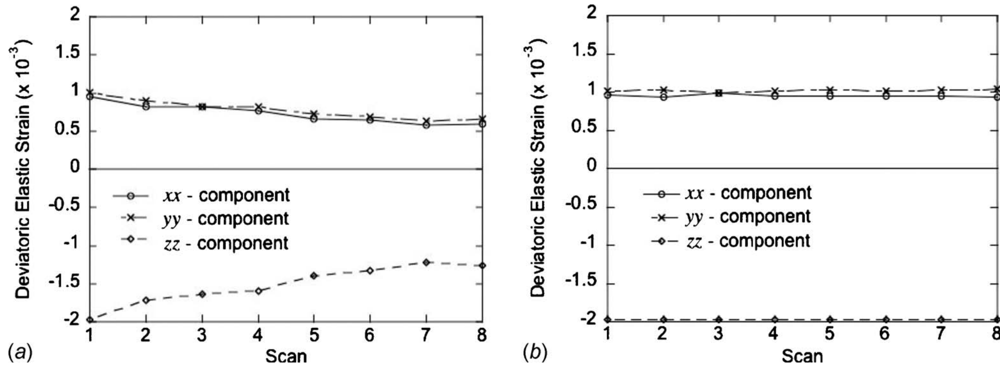

Fig. 6 Average normal deviatoric elastic strain components, (*a*) showing relaxation and (*b*) after adjusting to compensate for relaxation

standard error of the mean $\Sigma_{\varepsilon p}$ in the perpendicular deviatoric elastic strain, where overbar $\overline{(\ )}$ indicates average at the given pixel location over all the scans, which have data at that pixel and where $\Sigma_{\varepsilon p}$ is a measure of accuracy of $\bar{\varepsilon}_p$ determined from the scan to scan variability. The average value at a pixel can be considered as fluctuating from the average value over all the pixels due to true fluctuations resulting from microstructural variability and due to measurement error. Thus, we can write

$$\bar{\varepsilon}_p = \bar{\varepsilon} + \tilde{\varepsilon}_p^t + \tilde{\varepsilon}_p^e \tag{31}$$

where $\bar{\varepsilon} = \langle \bar{\varepsilon}_p \rangle$ is the average over all the pixels of $\bar{\varepsilon}_p$, $\tilde{\varepsilon}_p^t$ is the true fluctuation in ε from the mean at pixel p, and $\tilde{\varepsilon}_p^e$ is the fluctuation due to measurement error. Then, the standard deviations are related by

$$\Sigma_\varepsilon^2 = (\Sigma_\varepsilon^t)^2 + (\Sigma_\varepsilon^e)^2 \tag{32}$$

$$(\Sigma_\varepsilon^e)^2 = \frac{1}{N_p} \sum_{p=1}^{N_p} (\Sigma_{\varepsilon p})^2 \tag{33}$$

where Σ_ε is the standard deviation in $\bar{\varepsilon}_p$ over all the pixels. From the measurements, we can compute Σ_ε, which represents the spatial variability in the measurements (pixel to pixel variability) and Σ_ε^e, which represents the measurement error, is determined from Eq. (33). Then, using Eq. (32), we can estimate the true standard deviation in the perpendicular deviatoric elastic strain due to microstructural variability Σ_ε^t. We compare this to the predicted standard deviation in the perpendicular deviatoric elastic strain computed in the simulation Σ_ε^c. The results are shown in Table 2.

The predicted variability due to the microstructural effects Σ_ε^c is much less than the experimental value Σ_ε^t. Thus, the variability is due to more than just grain size and orientation effects captured in the crystal plasticity model. One source of discrepancy is due to neglecting initial elastic strains in the simulation. The standard deviation in the initial perpendicular deviatoric elastic strain, calculated from a single area scan prior to the thermal cycles, was $\Sigma_\varepsilon^b = 0.642 \times 10^{-3}$. Note that Σ_ε in Table 2 is the standard deviation in the pixel values computed from the average of eight area scans but if we compute the average standard deviation in the pixel variability from each of the eight area scans, we find this to be $\Sigma_\varepsilon^a = 0.782 \times 10^{-3}$, which could be considered as representing the average pixel variability for any single scan after the thermal cycles. Thus, while there is some increase in the variability after the thermal cycles due to the generation of thermal stress, the initial variability, created during the film deposition process and not eliminated in the annealing, is a substantial part of this. Additional discrepancies may be due to other idealizations in the model. For example, the film thickness and grain size effects, captured in Eqs. (8) and (9), treat these effects as being uniform over each grain rather than being stronger at the interfaces than in the interior. A strain gradient plasticity model would better reflect that intragranular variability. In addition, uniform film thickness and idealized boundary conditions may not accurately capture the full level of variability at the grain scale leading to an underprediction in the variability in the perpendicular deviatoric elastic strain.

Table 2 Standard deviations in perpendicular deviatoric elastic strain in units of 10^{-3}

Σ_ε	Σ_ε^e	Σ_ε^t	Σ_ε^c
0.5842	0.2169	0.5424	0.0813

To get a better idea of how the simulation and experimental measurements compare on a pixel by pixel basis, Figs. 7(*a*) and 7(*b*) compare the simulation and experimental results for the perpendicular deviatoric elastic strain in the film. While it is difficult to see much similarity between these, since the variability in the experiment is much greater, one observation is that the small grains in both images are primarily blue, indicating a more negative value of perpendicular deviatoric elastic strain, which would be associated with a higher in-plane stress. This is expected since smaller grains are stronger due to the Hall–Petch effect. The effect of grain size is discussed more in the next section.

4.3 Grain Size Effect. To investigate the grain size effect, we computed the average perpendicular, deviatoric elastic strain in grains of various sizes from the room temperature data and the simulation results. We considered only the grains on the interior, since we do not know the actual size of grains that are on the boundary and represent only a part of a grain. We computed the mean values by averaging the measurements at each pixel in all the grains of a given size where the grain size was determined by the number of pixels in the grain. The standard deviation was also computed for each grain size. The results are shown in Fig. 8 where linear curve fits are shown for the experiment and model and where the "error" bars are plus and minus one standard deviation (indicating variability for a given grain size due to both error and real variability). The linear curve fits for the experiment and model are in very good agreement. It is not surprising that the model fits a Hall–Petch relationship very well since this relationship is explicitly represented in the model in Eq. (9). The experimental data show more scatter from the linear Hall–Petch relationship, especially at the larger grain sizes, and much more variability is seen for each grain size in the experiment as illustrated by the large error bars.

Since the film has a strong $\langle 111 \rangle$ fiber texture, it is possible to approximately relate the perpendicular deviatoric elastic strain to the biaxial stress, assuming a random in-plane twist, as

Downloaded 08 Dec 2010 to 128.113.218.67. Redistribution subject to ASME license or copyright; see http://www.asme.org/terms/Terms_Use.cfm

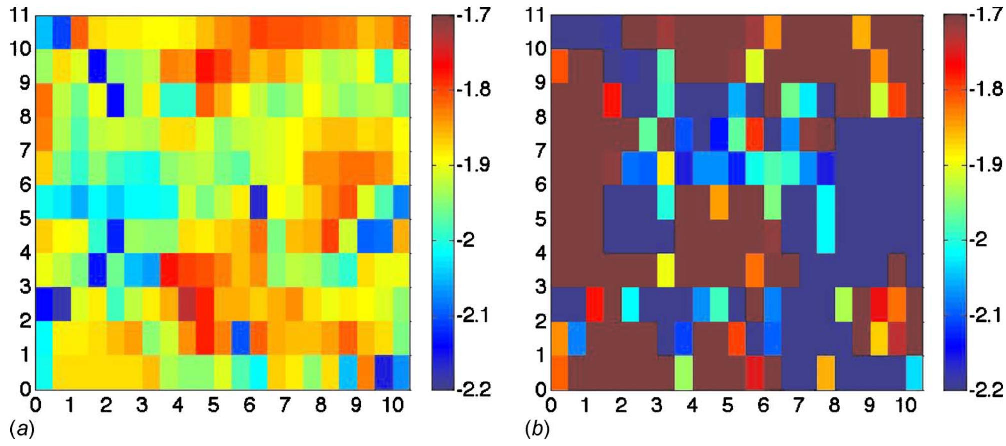

Fig. 7 Comparison of perpendicular deviatoric elastic strain resulting from (*a*) the simulation and (*b*) the experiment. The *x* and *y* scales are in μm and the color scale is in units of 10^{-3}. For the experimental results, the color scale is cropped to match that of the simulation, i.e., pixels with strains outside of the -2.2×10^{-3} to 1.7×10^{-3} range were assigned to corresponding end point strain values in (*b*).

$$\langle\sigma_b\rangle = -3C_{44}\langle\varepsilon_{zz}^{e'}\rangle \tag{34}$$

Using the above relationship and the linear curve fits from Fig. 8, we obtain the following relationships for the experiment and model (dropping the angle brackets), respectively

$$\sigma_b^m = 159.5\ \text{MPa} + \frac{18.7\ \text{MPa}\sqrt{\mu\text{m}}}{\sqrt{d}} \tag{35}$$

$$\sigma_b^c = 149.8\ \text{MPa} + \frac{20.6\ \text{MPa}\sqrt{\mu\text{m}}}{\sqrt{d}} \tag{36}$$

where superscript m indicates measured and c indicates computed. From this result, the Hall–Petch coefficient is predicted in the model to be $k^c=18.7\ \text{MPa}\sqrt{\mu\text{m}}=0.59\ \text{MPa}\sqrt{\text{mm}}$ and from the experiment $k^m=20.6\ \text{MPa}\sqrt{\mu\text{m}}=0.65\ \text{MPa}\sqrt{\text{mm}}$. This result can be compared with measurements of the Hall–Petch coefficient in Griffin et al. [3] who determined the Hall–Petch coefficient in free standing 1 μm thick Al–1%Si films of varying grain sizes subjected to biaxial stretching using a bulge test. They found the Hall–Petch coefficients at biaxial strains of 0.1%, 0.2%, and 0.4% to be $k=0.14\ \text{MPa}\sqrt{\text{mm}}$, $0.20\ \text{MPa}\sqrt{\text{mm}}$, and $0.43\ \text{MPa}\sqrt{\text{mm}}$, respectively. To compare with the experiments presented herein, the elastic-plastic biaxial strain at room temperature can be estimated from Eq. (1), where the applied biaxial strain ε_b in the film plane is assumed to be due to the thermal strain in the silicon, thus,

$$\varepsilon_b^e + \varepsilon_b^p = \varepsilon_b - \varepsilon_b^\theta = \int_{\theta_o}^{\theta}[\alpha_s(\theta') - \alpha(\theta')]d\theta' \tag{37}$$

Substituting in Eqs. (16) and (17) and taking $\theta_o=573$ K (300°C) and $\theta=298$ K (25°C) results in an effective applied elastic-plastic biaxial strain of 0.6%. Plotting the results here on the same graph with the measurements of Griffin et al. [3], Fig. 9, we see that the simulation and experimental results obtained here are in very good agreement with the measurements by Griffin et al.

Finally, it should be noted that other researchers, including Chaudhari [33] and Thompson [34], proposed that the flow stress in thin films is approximately inversely proportional to the grain size $(1/d)$ rather than the square root of the grain size $(1/\sqrt{d})$ as assumed here, Eq. (9). In their derivations, Chaudhari [33] and Thompson [34] considered the energy associated with dislocation segments that have to form in the grain boundaries, assuming columnar grain structures. Venkatraman and Bravman [4] considered both forms but found that their range of grain sizes considered combined with experimental errors were insufficient to conclusively infer which relationship was correct. It was found that the experimental results reported here fit the relationship proposed by Ashby [25] and used in the model presented here, Eq. (9), slightly better than the $(1/d)$ relationship. This is consistent with earlier work reported by Yu et al. [22]. However, as illustrated in

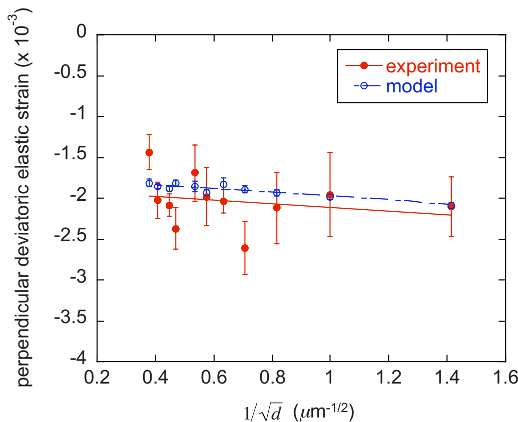

Fig. 8 Effect of the grain size on the perpendicular deviatoric elastic strain

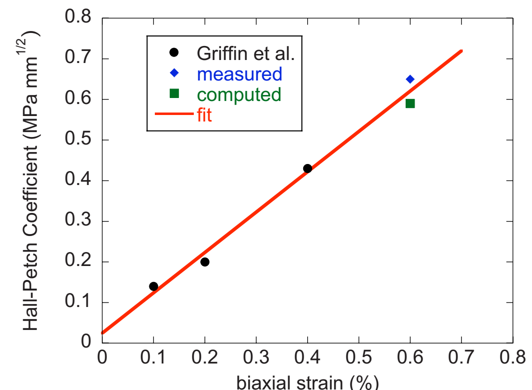

Fig. 9 Hall–Petch coefficient as a function of biaxial strain

Downloaded 08 Dec 2010 to 128.113.218.67. Redistribution subject to ASME license or copyright; see http://www.asme.org/terms/Terms_Use.cfm

Fig. 8, there is a lot of scatter in the experimental data; so, which form for the grain size effect is correct, it cannot be inferred conclusively from these data either.

5 Conclusions

X-ray microbeam measurements of deviatoric strain in an Al film subjected to two thermal cycles have been compared with a finite element model of the grain structure accounting for grain scale elastoviscoplastic behavior based on dislocation mechanisms. The finite element model considers film thickness, grain size, dislocation entanglement hardening, and grain orientation effects. At the film scale, considering the average biaxial stress in the film, the experiment and model are in fair agreement. At the subgrain scale, the experimentally observed deviatoric elastic strains exhibit considerably more variability than that predicted by the model. This is most likely primarily due to initial residual elastic strains in the film resulting from the film growth process, which are not included in the model and which have considerable variability. The effect of the grain size in the model and experiment match fairly well and the Hall–Petch coefficients are in good agreement with the experimental data on free standing Al thin films [3].

Acknowledgment

This material is based on work supported by the National Science Foundation under Grant No. DMR-0312189. The X-ray diffraction experiments were carried out on beamline 34-ID at the Advanced Photon Source, Argonne National Laboratory, which is supported by the United States Department of Energy.

References

[1] Vinci, R. P., and Vlassak, J. J., 1996, "Mechanical Behavior of Thin Films," Annu. Rev. Mater. Sci., **26**, pp. 431–462.
[2] Doerner, M., Gardner, D., and Nix, W., 1986, "Plastic Properties of Thin Films on Substrates as Measured by Submicron Indentation Hardness and Substrate Curvature Techniques," J. Mater. Res., **1**, pp. 845–851.
[3] Griffin, A. J., Jr., Brotzen, F. R., and Dunn, C., 1986, "Hall–Petch Relation in Thin Film Metallizations," Scr. Metall., **20**, pp. 1271–1272.
[4] Venkatraman, R., and Bravman, J. C., 1992, "Separation of Film Thickness and Grain Boundary Strengthening Effects in Al Thin Films on Si," J. Mater. Res., **7**, pp. 2040–2048.
[5] Nix, W. D., 1989, "Mechanical Properties of Thin Films," Metall. Trans. A, **20**, pp. 2217–2245.
[6] Thouless, M. D., 1995, "Modeling the Development and Relaxation of Stresses in Thin Films," Annu. Rev. Mater. Sci., **25**, pp. 69–96.
[7] Gerth, D., Katzer, D., and Krohn, M., 1992, "Study of the Thermal Behavior of Thin Aluminum Alloy Films," J. Appl. Phys., **67**, pp. 1831–1844.
[8] Kim, D.-K., Nix, W. D., Vinci, R. P., Deal, M. D., and Plummer, J. D., 2001, "Study of the Effect of Grain Boundary Migration on Hillock Formation in Al Thin Films," J. Appl. Phys., **90**, pp. 781–787.
[9] Sanchez, J. E., and Arzt, E., Jr., 1992, "Effects of Grain Orientation on Hillock Formation and Grain Growth in Aluminum Films on Silicon Substrates," Scr. Metall. Mater., **27**, pp. 285–290.
[10] Schwarzer, R. A., and Gerth, D., 1993, "Effect of Grain Orientation on the Relaxation of Thermomechanical Stress and Hillock Growth in Al-1%Si Conductor Layers on Silicon Substrates," J. Electron. Mater., **22**, pp. 607–610.
[11] Knorr, D. B., and Rodbell, K. P., 1996, "The Role of Texture in the Electromigration Behavior of Pure Aluminum Lines," J. Appl. Phys., **79**, pp. 2409–2417.
[12] Zielinski, E. M., Vinci, R. P., and Bravman, J. C., 1995, "Measurement of the Dependence of Stress and Strain on Crystallographic Orientation in Cu and Al Thin Films," Mater. Res. Soc. Symp. Proc., **356**, pp. 429–434.
[13] Wang, P.-C., Cargill, G. S., III, and Noyan, I. C., 1995, "Strain Measurements and Laue Diffraction With Microbeams," *Applications of Synchrotron Radiation Techniques to Materials Science II Symposium*, Materials Research Society, Pittsburgh, PA.
[14] Chung, J., and Ice, G., 1999, "Automated Indexing for Texture and Strain Measurements With Broad-Bandpass X-Ray Microbeams," J. Appl. Phys., **86**, pp. 5249–5255.
[15] Cargill, G. S., III, Moyer, L. E., Wang, G., Zhang, H., Hu, C.-K., Yang, W., Larson, B. C., and Ice, G. E., 2006, "Thermal and Electromigration-Induced Strains in Polycrystalline Films and Conductor Lines: X-Ray Microbeam Measurements and Analysis," AIP Conf. Proc., **816**, pp. 303–309.
[16] Freund, L. B., 1987, "The Stability of a Dislocation Threading a Strained Layer on a Substrate," ASME J. Appl. Mech., **54**, pp. 553–557.
[17] Pant, P., Schwarz, K. W., and Baker, S. P., 2003, "Dislocation Interactions in Thin FCC Metal Films," Acta Mater., **51**, pp. 3243–3258.
[18] von Blanckenhagen, B., Arzt, E., and Gumbsch, P., 2004, "Discrete Dislocation Simulations of Plastic Deformation in Metal Thin Films," Acta Mater., **52**, pp. 773–784.
[19] Fertig, R., and Baker, S. P., 2009, "Simulation of Dislocations and Strength in Thin Films: A Review," Prog. Mater. Sci., **54**, pp. 874–908.
[20] Povirk, G. L., Mohan, R., and Brown, S., 1995, "Crystal Plasticity Simulations of Thermal Stresses in Thin-Film Aluminum Interconnects," J. Appl. Phys., **77**, pp. 598–606.
[21] Eshelby, J. D., 1957, "The Determination of the Elastic Field of an Ellipsoidal Inclusion and Related Problems," Proc. R. Soc. London, Ser. A, **241**, pp. 376–396.
[22] Yu, J.-S., Maniatty, A. M., and Knorr, D. B., 1997, "Model for Predicting Thermal Stresses in Thin Polycrystalline Films," J. Mech. Phys. Solids, **45**, pp. 511–534.
[23] Cho, J.-H., Rollett, A. D., and Oh, K. H., 2005, "Determination of a Mean Orientation in Electron Backscatter Diffraction Measurements," Metall. Mater. Trans. A, **36**, pp. 3427–3438.
[24] Kocks, U. F., 1976, "Laws for Work-Hardening and Low-Temperature Creep," ASME J. Eng. Mater. Technol., **98**, pp. 76–85.
[25] Ashby, M. F., 1970, "The Deformation of Plastically Non-Homogeneous Materials," Philos. Mag., **21**, pp. 399–424.
[26] Frost, H. J., and Ashby, M. F., 1982, *Deformation-Mechanism Maps*, Pergamon, New York.
[27] Bassani, J., and Wu, T.-Y., 1991, "Latent Hardening in Single Crystals II. Analytical Characterization and Predictions," Proc. R. Soc. London, Ser. A, **435**, pp. 21–41.
[28] Touloukian, Y. S., Kirby, R. K., Taylor, R. E., and Desai, P. E., 1975, *Thermal Expansion, Metallic Elements, and Alloys*, IFI/Plenum, New York.
[29] Touloukian, Y. S., Kirby, R. K., Taylor, R. E., and Lee, T. Y. R., 1977, *Thermal Expansion—Nonmetallic Solids*, IFI/Plenum, New York.
[30] Every, A. G., and McCurdy, A. K., 1992. "Group III: Crystal and Solid State Physics: Elastic Constants," *Landolt-Börnstein Numerical Data and Functional Relationships in Science and Technology*, Vol. 29A, D. F. Nelson, ed., Spring-Verlag, Berlin, pp. 296–304.
[31] Ortiz, M., and Popov, E. P., 1985, "Accuracy and Stability of Integration Algorithms for Elastoplastic Constitutive Relations," Int. J. Numer. Methods Eng., **21**, pp. 1561–1576.
[32] Yang, C.-J., 2004, "Modeling Electromigration and Stress Driven Diffusion in Thin Metallic Films," Ph.D. thesis, Rensselaer Polytechnic Institute.
[33] Chaudhari, P., 1974, "Hillock Growth in Thin Films," J. Appl. Phys., **45**, pp. 4339–4345.
[34] Thompson, C. V., 1993, "The Yield Stress of Polycrystalline Thin Films," J. Mater. Res., **8**, pp. 237–238.

Downloaded 08 Dec 2010 to 128.113.218.67. Redistribution subject to ASME license or copyright; see http://www.asme.org/terms/Terms_Use.cfm